

Statistics of pressure fluctuations in turbulent kinetic plasmas

S. Adhikari^{1,2,★}, W. H. Matthaeus^{1,2,3}, T. N. Parashar^{1,2,4}, M. A. Shay^{1,2,3} and P. A. Cassak^{1,2,3}

¹Department of Physics and Astronomy, West Virginia University, Morgantown, West Virginia 26506, USA

²Department of Physics and Astronomy, University of Delaware, Newark, Delaware 19716, USA

³Bartol Research Institute, Department of Physics and Astronomy, University of Delaware, Newark, Delaware 19716, USA

⁴School of Chemical and Physical Sciences, Victoria University of Wellington, Wellington 6140, New Zealand

Accepted 2023 September 18. Received 2023 September 15; in original form 2023 April 19

ABSTRACT

In this study, we explore the statistics of pressure fluctuations in kinetic collisionless turbulence. A 2.5D kinetic particle-in-cell simulation of decaying turbulence is used to investigate pressure balance via the evolution of thermal and magnetic pressure in a plasma with β of order unity. We also discuss the behaviour of thermal, magnetic, and total pressure structure functions and their corresponding wavenumber spectra. The total pressure spectrum exhibits a slope of $-7/3$ extending for about a decade in the ion-inertial range. In contrast, shallower $-5/3$ spectra are characteristic of the magnetic pressure and thermal pressure. The steeper total pressure spectrum is a consequence of cancellation caused by density-magnetic field magnitude anti-correlation. Further, we evaluate higher order total pressure structure functions in an effort to discuss intermittency and compare the power exponents with higher order structure functions of velocity and magnetic fluctuations. Finally, applications to astrophysical systems are also discussed.

Key words: hydrodynamics – MHD – plasmas – turbulence.

1 INTRODUCTION

1.1 Motivation

Most naturally occurring as well as laboratory plasma flows are turbulent. Astrophysical systems of interest include the intracluster medium (ICM) (Schuecker et al. 2004; Churazov et al. 2012; Zhuravleva et al. 2014, 2019), black hole accretion discs (Balbus & Hawley 1998; Pessah 2010), solar wind (Coleman 1968; Matthaeus & Goldstein 1982; Bruno & Carbone 2013), and planetary magnetospheres (Sahraoui, Hadid & Huang 2020). Turbulent stresses and pressure play an important role at scales ranging from the largest structures in the Universe (Simionescu et al. 2019) to laboratory plasmas. A prominent feature of galactic plasma observations is the ‘great power-law’ spectrum of electron density fluctuations that extends over more than ten orders of magnitude in scale (Armstrong, Cordes & Rickett 1981) in the interstellar medium. Under mild assumptions (Montgomery, Brown & Matthaeus 1987) this spectrum is found to be consistent with Kolmogorov spectrum of magnetic field fluctuations. This calculation depends on an assumption of near-incompressibility and also implies that density and magnetic field, and therefore mechanical and magnetic pressures, are anticorrelated and partially cancel one another. This kind of *statistical pressure balance* is an element of turbulent dynamics, in contrast to the superficially similar *static pressure balances* that are special solutions of the ideal magnetohydrodynamics (MHD) equations.

Pressure balance plays an important role in astrophysics. The mass of galaxy clusters (Kravtsov & Borgani 2012; Planck et al. 2013; Schleicher &

Bykov 2015), the largest structures in the Universe, provides stringent constraints on cosmological models (Carlberg et al. 1997; Voigt & Fabian 2006; Pratt et al. 2019). Hydrostatic pressure balance is a common assumption used to estimate the mass of relaxed clusters (Lau, Nagai & Nelson 2013). However, this assumption can easily break in clusters far from equilibrium and can also be broken by turbulent stress contributions (Markevitch et al. 2004; Angelinelli et al. 2020). X-ray (Schuecker et al. 2004; Churazov et al. 2012; Zhuravleva et al. 2014) and radio observations via the Sunayev-Zel’dovich (Khatri & Gaspari 2016) effect provide detailed measurements of the thermal properties of galaxy clusters. An accurate understanding of the pressure dynamics in the intracluster medium can help disentangle contributions from thermal pressure and turbulent stresses.

Similarly, properties of the pressure have a major impact in the heliosphere. Near-Earth, the solar wind plays a vital role in shaping Earth’s magnetosphere and driving space weather. The solar wind is measured to be turbulent (Coleman 1968; Matthaeus & Goldstein 1982; Bruno & Carbone 2013) and is observed to be hotter than expected from adiabatic cooling (Wang & Richardson 2001; Hellinger et al. 2013). Heating implies an increase of the trace of the pressure tensors, and this increase in the internal energy occurs through interaction between the pressure tensors and the velocity gradient tensors (Yang et al. 2017a). The solar wind routinely displays intervals of pressure balance (Vellante & Lazarus 1987; Goldstein, Roberts & Matthaeus 1995; Reisenfeld, McComas & Steinberg 1999; Ruffolo et al. 2021) which potentially emerge as a result of the nearly incompressible MHD (NI-MHD) of the solar wind (Matthaeus et al. 1991).

In this study, we develop a framework to discuss pressure balance in the context of the equation governing pressure in incompressible MHD with and without shear. We also explore various aspects of

* E-mail: subash.adhikari@mail.wvu.edu

pressure dynamics in kinetic plasmas using a fully kinetic particle-in-cell (PIC) simulation. We find that the pressure spectrum follows the hydrodynamic scaling in the incompressible MHD regime. Although the kinetic plasmas are not fully incompressible, the pressure spectrum shows an excellent agreement with the power scaling following the MHD predictions, indicating that the simulation is likely in a state of NI-MHD. The remaining paper is organized as follows: Section 2 first reviews some additional theoretical background and then constructs the Poisson's equation for pressure in an incompressible MHD framework. In Section 3 we report the results from PIC simulation, and finally we discuss the implications and future directions in Section 4.

2 THEORY

2.1 Background

Following the seminal work on hydrodynamic pressure fluctuations by Obukhoff and Batchelor (Batchelor 1951; Obukhoff & Yaglom 1951), the second-order pressure structure function D_p^2 and pressure spectrum have been studied both experimentally (Uberoi 1953; George, Beuther & Arndt 1984; Tsuji & Ishihara 2003) and via direct numerical simulations (Schumann & Patterson 1978; Kim & Antonia 1993; Pullin & Rogallo 1994; Nelkin & Chen 1998; Squire et al. 2023), mostly for homogeneous and isotropic turbulence. All these studies rely on the assumptions that the velocity distribution is joint Gaussian or the small-scale statistics follow Kolmogorov's similarity hypothesis such that D_p^2 as a function of lag r is proportional to $r^{4/3}$. Therefore, the pressure spectrum $E_p(k)$ varies as $k^{-7/3}$ within the inertial range, where k is the wavenumber. Attempts have also been made to extend the pressure spectrum to the higher wavenumber (dissipation range) (Zhao et al. 2016). However, the kinetic/dissipation range scaling exponents are less well understood, in general and for the pressure spectrum.

The study of nearly incompressible MHD (Klainerman & Majda 1981) is a bit more subtle than the hydro case. Beginning with the Montgomery et al. (1987) explanation of the $k^{-5/3}$ spectrum of the interstellar density structure function, several additional layers of theory have been presented (Higdon 1984; Matthaeus & Brown 1988a) based on the idea that the core solution of the plasma dynamics in a perturbation theory controlled by the turbulent Mach number is incompressible MHD, and the leading order density fluctuations are those discussed by Montgomery et al. (1987). Additional theories have been presented that elaborate on the role of thermal fluctuations (Zank & Matthaeus 1990; Bayly, Levermore & Passot 1992), and variations in plasma beta (Zank & Matthaeus 1992, 1993). In light of the latter references, the original perturbation theory of Montgomery et al. (1987) and Matthaeus & Brown (1988a) can be seen to apply most readily to plasma beta greater than unity.

To place the current work better in the context of these prior studies, it is important to emphasize that most of the literature focuses on mechanical pressure statistics in both hydrodynamic turbulence and MHD. Then mechanical pressure is linked to density and thermal fluctuations through an equation of state. In contrast, this study is mainly concerned with statistics of the total pressure – magnetic plus mechanical – and contrasting this with behaviour of the magnetic and mechanical pressure separately. Therefore, we are concerned with pressure balances. We will also examine higher order statistics related to total pressure. Notably we will study in detail these properties using a particle-in-cell model of collisionless plasma, thus departing substantially from the starting point of the MHD model.

2.2 Pressure Poisson's equation in MHD

The incompressible MHD equations (using Einstein's convention) are given by

$$\partial_t u_i + u_j \partial_j u_i - b_j \partial_j b_i = -\partial_i P + \nu \partial_j \partial_j u_i, \quad (1)$$

$$\partial_t b_i + u_j \partial_j b_i - b_j \partial_j u_i = \eta \partial_j \partial_j b_i, \quad (2)$$

where \mathbf{u} is the flow velocity, \mathbf{b} is the magnetic field in Alfvén units, P is the total pressure (magnetic plus thermal), ν is the kinematic viscosity, and η is the electric diffusivity. Here, the density is assumed to be unity and the velocity is solenoidal $\nabla \cdot \mathbf{u} = 0$. Now, in terms of Elsässer variables \mathbf{z}^\pm defined as $\mathbf{z}^\pm = \mathbf{u} \pm \mathbf{b}$, the above equations can be combined as:

$$\partial_t z_i^\pm + z_j^\mp \partial_j z_i^\pm = -\partial_i P + \nu \partial_j \partial_j z_i^\pm, \quad (3)$$

where we assume $\nu = \eta$. Taking the divergence of equation (3) and employing incompressibility ($\partial_i z_i = 0$) we get

$$-\partial_{ii} P = \partial_i (z_j^\mp \partial_j z_i^\pm) = (\partial_i z_j^\mp)(\partial_j z_i^\pm). \quad (4)$$

As written, the pressure is now seen to be as a constraint force that acts to maintain the solenoidal nature of the velocity field. The so-called *Nearly Incompressible MHD* theory proceeds to compute the density as a linear response to the pressure fluctuations (Batchelor 1951; Montgomery et al. 1987; Matthaeus & Brown 1988b) that emerge from the solution of equation (4).

Incompressibility does not imply constant pressure in the system, as seen in equation (4); instead, pressure is a non-linear function of the Elsässer variables suggesting any fluctuation in the Elsässer variable creates a pressure field in the system and vice-versa. The right-hand side of equation (4) can be split into symmetric and anti-symmetric (skew-symmetric) parts as

$$-\partial_{ii} P = (\partial_i z_j^\mp)(\partial_j z_i^\pm) = (\tau_{ij}^\mp + R_{ij}^\mp)(\tau_{ij}^\pm - R_{ij}^\pm), \quad (5)$$

where $\tau_{ij}^\pm = \frac{1}{2}(\partial_i z_j^\pm + \partial_j z_i^\pm)$ is the symmetric part of the decomposition, and is called the rate of strain tensor related to the Elsässer's variable, while $R_{ij}^\pm = \frac{1}{2}(\partial_i z_j^\pm - \partial_j z_i^\pm)$ is the anti-symmetric component, called the rate of rotation tensor associated with the curl of the Elsässer variable. One can simplify equation (5) further to obtain

$$-\partial_{ii} P = \tau_{ij}^- \tau_{ij}^+ - R_{ij}^- R_{ij}^+. \quad (6)$$

The first term on the right-hand side is related to the strain tensor. If one decomposes τ_{ij}^\pm such that $S_{ij} = \frac{1}{2}(\partial_i u_j + \partial_j u_i)$ and $M_{ij} = \frac{1}{2}(\partial_i b_j + \partial_j b_i)$ are the velocity and magnetic rates of strain respectively, then $\tau_{ij}^- \tau_{ij}^+ = S_{ij} S_{ij} - M_{ij} M_{ij} = S^2 - M^2$, where S^2 and M^2 are the respective squares of the velocity and magnetic rate of strain tensors. These are the associated second tensor invariants, equal to the sum of squares of the respective eigenvalues.

The second term on the right-hand side simplifies further to yield $R_{ij}^- R_{ij}^+ = \frac{1}{4}(\nabla \times \mathbf{z}^-)_k (\nabla \times \mathbf{z}^+)_k = \frac{1}{4}(\omega_k - j_k)(\omega_k + j_k) = \frac{1}{4}(\omega_k \omega_k - j_k j_k)$, where $\boldsymbol{\omega} = \nabla \times \mathbf{u}$ is the vorticity and $\mathbf{j} = \nabla \times \mathbf{b}$ is the current density. Therefore, equation (6) can be re-written as:

$$-\partial_{ii} P = (S^2 - M^2) - \frac{1}{4}(\omega_i \omega_i - j_i j_i). \quad (7)$$

Equation (7) is the Poisson equation for pressure, which shows that the pressure fluctuations are related to the rate of velocity and magnetic field strains and their rotations. In the absence of a magnetic field, equation (7) reduces to $-\partial_{ii} P = S^2 - \frac{1}{4}\omega_i \omega_i$.

At this point, it is useful to remind the reader that our approach is to examine the behaviour of a kinetic plasma in the nearly incompressible limit, at moderate, order unity, plasma β , and at

low turbulent Mach number. In this regime, we can apply a strategy analogous to that of Montgomery et al. (1987), to study the behaviour of the scalar pressure in some detail in the following sections. However one may also inquire concerning the behaviour of *pressure anisotropy*, including in principle gyrotropic and non-gyrotropic effects (Swisdak 2016; Yang et al. 2023), anisotropy-driven instabilities (Gary 1993; Bale et al. 2009; Verscharen, Klein & Maruca 2019; Qudsi et al. 2020), and collisionless dissipation channels (Yang et al. 2022). Each of these requires major efforts considerably beyond the scope of this work and we refer the reader of the literature for progress in these areas. However, we note that for the present case of plasma beta (β) ~ 1 and turbulent Mach number < 1 we expect pressure anisotropies to be present, but not significant enough to alter the anticorrelation between thermal and magnetic pressure. On the other hand, for completeness we include a few basic results on plasma pressure anisotropies in the Appendix B. For more details on pressure anisotropy, the readers are referred to these recent articles by Squire, Quataert & Kunz (2017), Bott et al. (2021), Arzamasskiy et al. (2023), Ley et al. (2023), Squire et al. (2023), Tran et al. (2023), and the references therein.

2.3 Poisson's equation with shear

Using Reynolds' decomposition, we can write a physical quantity (say P) as the sum of mean (\bar{P}) and fluctuating component (\tilde{P}). Substituting in equation (4), and using $\partial_i \tilde{z}_i^\pm = 0$, we get

$$\partial_{ii} \bar{P} + \partial_{ii} \tilde{P} = -\partial_i \partial_j (\bar{Z}_i^\mp \bar{Z}_j^\pm + \bar{Z}_i^\mp \tilde{Z}_j^\pm + \tilde{Z}_i^\mp \bar{Z}_j^\pm + \tilde{Z}_i^\mp \tilde{Z}_j^\pm). \quad (8)$$

Subtracting the ensemble average from itself we get

$$\partial_{ii} \tilde{P} = -\partial_i \partial_j (\bar{Z}_i^\mp \tilde{Z}_j^\pm + \tilde{Z}_i^\mp \bar{Z}_j^\pm) - \partial_i \partial_j (\tilde{Z}_i^\mp \tilde{Z}_j^\pm - \bar{Z}_i^\mp \bar{Z}_j^\pm), \quad (9)$$

which is the shear form of the Poisson equation for fluctuations in pressure.

The form of equation (9) is the same as its hydrodynamic counterpart except that u is replaced by z . Clearly, the Laplacian of pressure fluctuation is composed of two different terms. The first term represents the distortion produced by the shear as a result of interaction of shear with turbulence, while the second term is the interaction among the turbulent fluctuations. Solving equations (7) and (9) for pressure requires specific boundary conditions which is out of scope of this paper. Instead, we focus ourselves on the statistics of pressure, as follows. The characteristics of pressure fluctuation can be studied using the pressure correlation functions $R_P(\mathbf{r}) = \langle P(\mathbf{x} + \mathbf{r})P(\mathbf{x}) \rangle$ (Batchelor 1951) or the second-order pressure structure functions $D_P^2(\mathbf{r}) = |\delta P(\mathbf{r})|^2$ (Obukhoff & Yaglom 1951) both of which are related to each other (Monin & Yaglom 1975). Here, \mathbf{x} represents the positions space, \mathbf{r} represents the spatial lag, $\langle \dots \rangle$ represents the ensemble average, and the pressure increment is defined as $\delta P(\mathbf{r}) = P(\mathbf{x} + \mathbf{r}) - P(\mathbf{x})$.

The scaling of the pressure spectrum in the inertial range can be readily identified by applying Kolmogorov similarity hypothesis to pressure increments (Kolmogorov 1991). The second-order structure function $D_P^2(r)$ depends only on spatial lag r and rate of dissipation of energy ϵ , and can be written as

$$D_P^2(r) = \langle |P(\mathbf{x} + \mathbf{r}) - P(\mathbf{x})|^2 \rangle = C_p \epsilon^{4/3} r^{4/3}, \quad (10)$$

where C_p is a constant. The form in equation (10) is valid in the inertial range. A Fourier transform of equation (10) results in the pressure spectrum $E_P(k)$ with the mathematical form

$$E_P(k) \propto \epsilon^{4/3} k^{-7/3}, \quad (11)$$

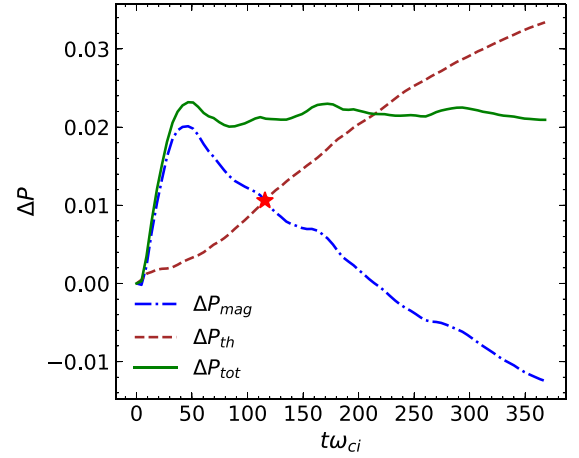


Figure 1. Time evolution of the change in thermal P_{th} , magnetic P_{mag} , and total pressure P_{tot} calculated with respect to their initial values. P_{mag} and P_{th} have opposite behaviour once the magnetic pressure reaches the maximum value. The red star represents the time of analysis.

where k is the wavenumber. The second-order pressure structure function has also been linked to the fourth-order velocity structure function (Hill & Wilczak 1995; Hill & Boratav 1997; Nelkin & Chen 1998) and a mixed third-order structure function of pressure gradient and velocity (Hill & Boratav 2001). However, exploring such relationship is beyond the scope of this paper, where our emphasis is on kinetic plasmas.

3 SIMULATION AND RESULTS

To study the statistics of pressure fluctuations in kinetic plasmas, we analyse a 2.5D fully kinetic PIC simulation of turbulence performed using the P3D code (Zeiler et al. 2002). The simulation follows the normalization where length is normalized to the ion-inertial length $d_i = c/\omega_{pi}$, where c is the speed of light and ω_{pi} is the plasma frequency for ions; time is normalized to the inverse of the cyclotron frequency ω_{ci} and velocity is normalized to Alfvén speed $v_{A0} = B_0/\sqrt{4\pi m_i n_0}$, where m_i is the mass of ions, B_0 and n_0 are the normalizing parameters for magnetic field and number density, respectively. Similarly, temperature is normalized to $m_i v_{A0}^2$ and pressure is normalized to $n_0 m_i v_{A0}^2$.

The simulation is a periodic square domain of length $L = 149.6d_i$ with grid points of 4096^2 , and 3200 particles initially in each grid. The mass ratio of ions to electrons is set to 25 with an initial background density of 1, uniform initial temperature of $T_e = T_i = 0.3$ with a total plasma beta $\beta = 1.2$, and an initial out-of-plane magnetic field of strength 1. The speed of light $c = 15v_{A0}$ and the system is initially populated with Fourier modes for magnetic field and velocity (both ions and electrons) within $2k_0 \leq |k| \leq 4k_0$, where $k_0 = 2\pi/L$ and allowed to evolve for about $370t\omega_{ci}$ without external forcing (see Parashar, Matthaeus & Shay 2018; Adhikari et al. 2021 for details).

3.1 Pressure balances

Fig. 1 shows the time evolution of the ensemble averaged (i.e. volume integrated) change in magnetic ΔP_{mag} and total thermal ΔP_{th} pressure. The change in the pressure is calculated with respect to the initial value at $t = 0$. Initially, the magnetic pressure increases rapidly for a small period of time and then falls, while the thermal pressure continues to increase gradually throughout the simulation. Note, the

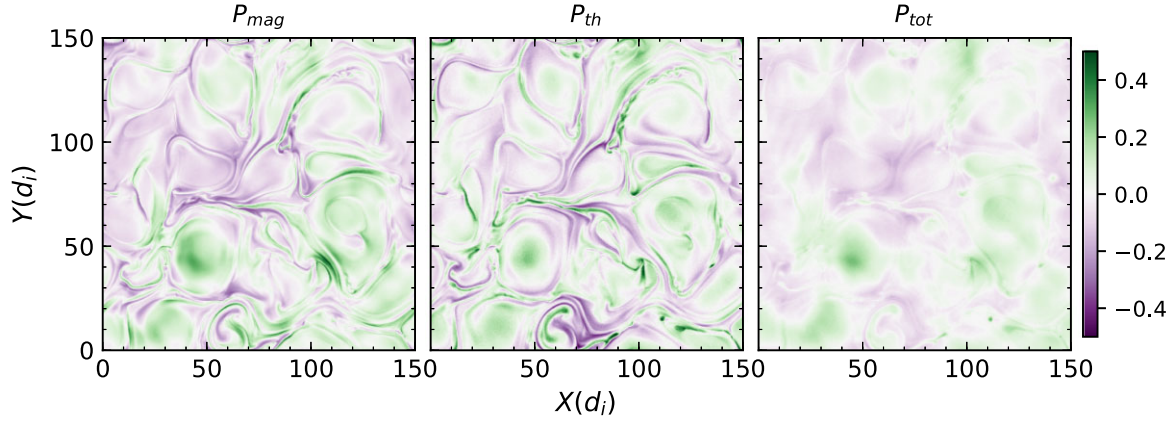


Figure 2. Two dimensional image at $t\omega_{ci} = 116.5$ of the magnetic P_{mag} , thermal P_{th} , and total P_{tot} pressure fluctuations normalized to their respective mean values.

Table 1. Variance about the spatial mean of the magnetic, thermal, and total pressure as plotted in Fig. 2.

Variance	P_{th}	P_{mag}	P_{tot}
σ^2	0.0107	0.0101	0.0039

change in the total pressure stays roughly constant once it reaches the maximum value; as the thermal pressure compensates for the fall in the magnetic pressure. The change in the magnetic and thermal pressure intersects at $t\omega_{ci} = 116.5$ when the mean square current is maximum in the system (not shown). This time, when MHD dissipation typically reaches a maximum, is often regarded as the turbulence having reached a fully developed state. One finds that in this state, the volume-integrated magnetic pressure and the volume-integrated thermal pressure are anticorrelated, producing a near-constant volume integrated total pressure. Since we are interested in the turbulence properties of pressure fluctuations, we focus our analysis around this time.

To understand how the global pressure balance impacts the local pressures, in Fig. 2 we show the two-dimensional view of the thermal, magnetic, and total pressure fluctuations at $t\omega_{ci} = 116.5$, each normalized to their respective mean value. It is observed that most of the regions near the current sheets (see Fig. A1) have low magnetic pressure and high thermal pressure indicating a negative correlations between the two. As a result the total pressure in these regions stay relatively uniform as seen on the right panel of Fig. 2. On the other hand, the magnetic islands have similar magnitude of P_{mag} and P_{th} . This is certainly due to the magnetic compression and heating within the islands. The total pressure balance is further quantified by calculating the variance of the pressure fluctuations plotted in Fig. 2, and is shown in Table 1. The variance of the magnetic and thermal pressure fluctuations have similar magnitude, while the variance of the total pressure fluctuation is much smaller (~ 40 per cent of P_{th} or P_{mag}).

Next, we plot the joint probability distribution function (PDF) of the thermal and magnetic pressure in Fig. 3, where a line of slope -1 is drawn for reference. The joint PDF clearly follows the reference line suggesting a negative correlation between the two pressures. In addition, we compute the Pearson correlation coefficient r_p (Cohen et al. 2009) between P_{th} and P_{mag} to be -0.257 supporting the trend seen in Fig. 3. This anti-correlation quantifies the tendency towards statistical (in contrast to pointwise) pressure balance. However, one might be tempted to ask at what scales are

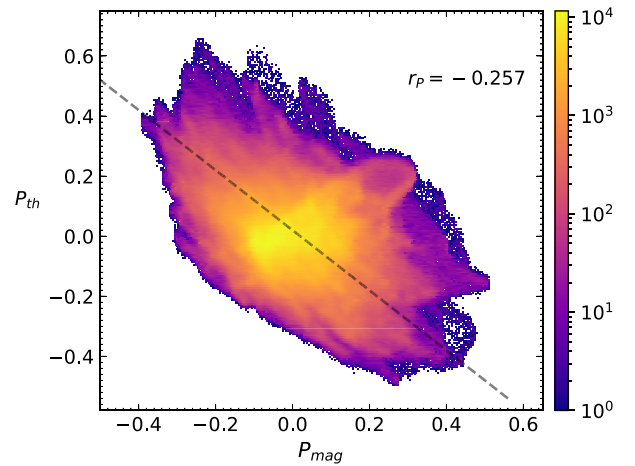


Figure 3. Joint probability distribution of the thermal P_{th} and magnetic P_{mag} pressure at $t\omega_{ci} = 116.5$. A dashed line of slope -1 is drawn for reference and r_p represents the Pearson correlation coefficient.

these correlations significant. In order to answer the question, we study the behaviour of the observed correlation as a function of lag scales using scale-filtering (Germano 1992), a technique often used to disentangle the structures in turbulence. In this technique, any field $f(\mathbf{x}, t)$ can be filtered at a scale ℓ using a proper filtering kernel $G_\ell(\mathbf{r}) = \ell^{-d}G(\mathbf{r}/\ell)$. Here $G(\mathbf{r})$ is a normalized, non-negative boxcar window function and d is the spatial dimension. Now, the filtered field \tilde{f}_ℓ at scale ℓ is given by $\tilde{f}_\ell(\mathbf{x}, t) = \int d^d r G_\ell(\mathbf{r}) f(\mathbf{x} + \mathbf{r}, t)$. Clearly, this is a low pass filter and therefore the filtered function $\tilde{f}_\ell(\mathbf{x}, t)$ only contains information at scales $\geq \ell$. Yet, one can approximate the information at scale ℓ simply using the difference between two filtered functions $\tilde{f}_{\ell+\Delta\ell}(\mathbf{x}, t) - \tilde{f}_{\ell-\Delta\ell}(\mathbf{x}, t)$. Here, $\Delta\ell$ is chosen to be the grid resolution of the simulation. Once the filtering has been applied to the thermal and magnetic pressures, we compute the Pearson correlation coefficient between them, and the result is shown in Fig. 4. It is found that there is no correlation between P_{th} and P_{mag} at smallest scales. However, as the lag scale ℓ increases there develops some anti-correlation and at scales $\approx d_i$ there is almost a perfect anti-correlation between the magnetic and thermal pressure. As lag increases, the anti-correlation falls, and at scales $\geq 30\text{code}$, P_{th} and P_{mag} are found to be positively correlated. The ion and electron thermal pressure also exhibits similar correlation trend with the magnetic pressure.

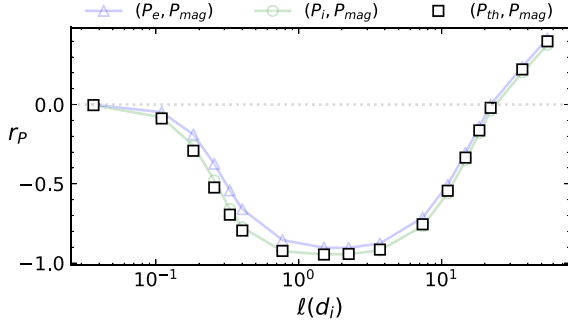


Figure 4. Pearson correlation coefficient r_p between the thermal and magnetic pressure as a function of scales. All the electrons (blue triangles), ions (green circles), and the total (black squares) thermal pressure have significant negative correlation at scales $\sim d_i$ (see text for more details).

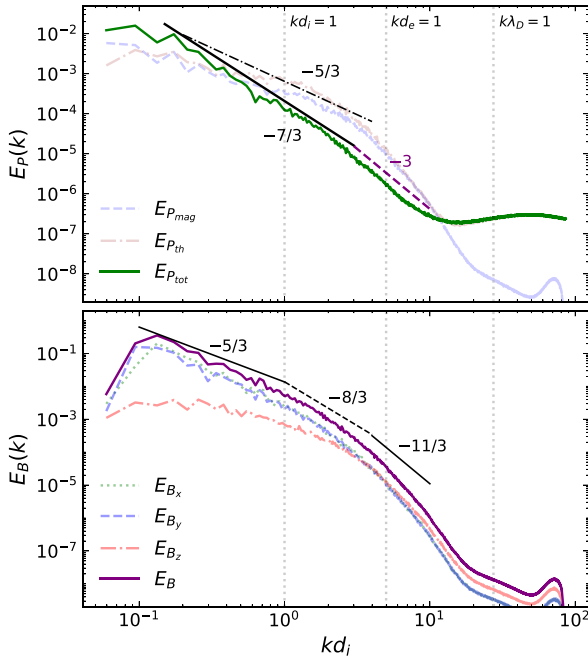


Figure 5. (Top) Pressure spectra for magnetic pressure (dashed line), thermal pressure (dash-dot) and total pressure (solid green line) as a function of wavenumber at the time of analysis. Reference lines with slopes $-5/3$, $-7/3$, and -3 are provided. (Bottom) Magnetic energy spectra at the same time. Lines of slope $-5/3$, $-8/3$, and $-11/3$ are drawn for reference. Both total spectrum and component spectra are shown (See legend).

We now discuss the pressure spectra. In the top panel of Fig. 5, we plot the magnetic, thermal, and total pressure spectra. The dotted vertical lines represent the wavenumber corresponding to the ion inertial length d_i^{-1} , electron inertial length d_e^{-1} , and the Debye length λ_D^{-1} . Additional lines of slope $-5/3$, $-7/3$, and -3 are drawn for reference. The thermal and magnetic pressure spectra exhibit very similar behaviour except at the higher wavenumbers. In the inertial range $k d_i \lesssim 1$, both these spectra exhibit similar spectral slopes close to $-5/3$, while at large wavenumbers $k d_i > 5$, the thermal pressure has a plateau at approximately 10^{-7} while the magnetic pressure spectrum falls down below 10^{-8} .

Once again, the total pressure displays different behaviour compared to its constituent parts. The total pressure spectrum, in the inertial range displays a spectral slope of $-7/3$ consistent with equation (11). This is due to the significant cross-spectrum correlation

between the thermal and the magnetic pressure, a direct consequence of the statistical pressure balance described above.

At higher wavenumber, the total pressure spectrum steepens beyond the inertial range $2 \leq k d_i \leq 9$ with slope -3 before the hump on the thermal pressure spectrum dominates the contribution.

The bottom panel of Fig. 5 shows the magnetic energy spectra along with its components. In the inertial range ($k d_i \lesssim 1$) the magnetic spectra approximate the familiar Kolmogorov $-5/3$ slope as expected in strong turbulence. Near $k d_i = 1$ the magnetic spectra steepen, as often reported for plasma (Leamon et al. 1998), with a slope that varies in the range of about $-7/3$ to $-8/3$ (Smith et al. 2006). In this range kinetic dissipation and dispersion effects become important. Various steeper forms have been proposed for the spectrum at still higher wavenumbers $k d_e > 1$; an $11/3$ spectrum is shown here for reference. The spectrum of the out of plane component B_z is much flatter than the other two magnetic components, and in the inertial range appears at a much lower amplitude, down by as much as two orders of magnitude at the long wavelength end of the inertial range. However at the intermediate kinetic range, the B_z spectrum reaches equipartition with the spectra of the other two components, and further along, at sub electron scales, this component becomes dominant over the other two by a modest factor.

We note in passing that the theoretical development in (Montgomery et al. 1987) began with assumption that the magnetic spectrum exhibits a $-5/3$ spectrum and proceeded to compute the density and pressure spectra as a linear response to the magnetic field. The conclusion was that in MHD the thermal pressure (and density) spectra would take on a $-5/3$ power law as seen here. The anti-correlation of thermal and magnetic pressure at inertial range scales was also concluded. The statistical characterization of total pressure was not included. The present findings are complementary to this important antecedent.

Next, we show the probability density function (PDF) of the pressure increments (δP) defined in Section 2.3 as:

$$\delta P(\mathbf{r}, \mathbf{x}) = P(\mathbf{x} + \mathbf{r}) - P(\mathbf{x}), \quad (12)$$

where \mathbf{r} is the spatial lag. For simplicity, we compute the PDF using lags along the x and y directions, and average the results. One can also perform these calculations for lags along different directions and take an angular average (Wang et al. 2022). The PDF's are shown in Fig. 6 for two different lags $r = 1 d_e \approx 0.2 d_i$ (left panel) and $r \approx 1 d_i$ (right panel).

At $r \approx d_i$, the PDF of both δP_{mag} (blue circles) and δP_{th} (red diamonds) follow each other closely in contrast to the $r \approx d_e$ case, however, displaying a departure from Gaussianity in both cases. The total pressure PDF (green box) for $r \approx d_e$ is very close to a normal distribution (solid black line), drawn for reference, but is distorted for $r \approx d_i$ implying better pressure balance at smaller lags.

To examine the spatial distributions that originate from different sections of these PDF's, we divide the probability distribution function into regions I, II, and III (as in Greco et al. 2009) and mask out all but one region in a given plot. The results for small lag increments, at $r \approx d_e$, are shown in Fig. 7. Here, we have used a binary colour representation where black represents the structures contributing to a particular region, and white represents the region with no contribution. It is immediately evident that the total pressure increments at this scale are much more homogeneous than the separate contributions from magnetic or thermal pressures. This is the case for the region I core of the distributions, for the fine scale super-Gaussian tails representing region III, and for the intermediate subGaussian regions II. This signature of pressure balance is particularly clear for the superGaussian tail. However, none of

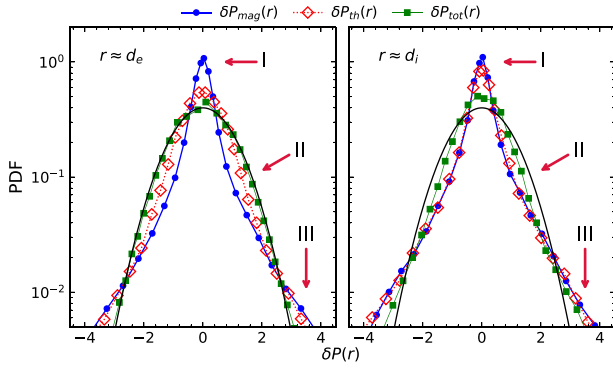


Figure 6. Probability density functions of pressure increments δP , for magnetic pressure (blue circles), thermal pressure (red diamonds), and total pressure (green boxes), each normalized by its standard deviation, at $r \approx 1d_e = 0.2d_i$ (left), and $r \approx 1d_i$ (right). These PDFs are calculated at $t = 116.5\omega_{ci}^{-1}$ for lags along both x and y axes, and the results are averaged. The black solid line is a normal distribution for reference (see text for details).

these regions is completely uniform. In fact the spatial distribution of magnetic islands and their boundaries, i.e. what we sometimes called cellularization of the plasma (Servidio, Matthaeus & Dmitruk 2008), is evident in all three ranges of the PDF, as is evident in the panels of Fig. 7. Quantitative diagnostics of this spatial structure leads us to a discussion of *intermittency*.

Theories and classifications of intermittency provide a physical basis for quantifying deviations from Gaussianity. To understand the intermittency of pressure fluctuations, we calculate the scale-dependent kurtosis and higher-order structure function for pressure increments in the following sub-section.

3.2 Higher order statistics and intermittency

3.2.1 Scale-dependent kurtosis

The scale-dependent kurtosis $\kappa(\mathbf{r})$ for the pressure fluctuations $\delta P(\mathbf{r})$ as a function of lag \mathbf{r} is defined as:

$$\kappa(\mathbf{r}) = \frac{\langle |P(\mathbf{x} + \mathbf{r}) - P(\mathbf{x})|^4 \rangle}{\langle |P(\mathbf{x} + \mathbf{r}) - P(\mathbf{x})|^2 \rangle^2}. \quad (13)$$

$\kappa(\mathbf{r})$ takes on a value of three for a scalar field having a Gaussian distribution. For a scalar quantity (or its increments) less randomly distributed and more clustered in space, $\kappa(\mathbf{r})$ attains larger values, and can be heuristically interpreted as the reciprocal of the spatial filling factor. This property makes $\kappa(\mathbf{r})$ a good preliminary indicator of the presence of spatial intermittency.

In Fig. 8, we plot $\kappa(r)$ for magnetic, thermal, and total pressure. It is observed that $\kappa(r)$ is non-Gaussian for all pressure forms at the smaller lags $r \leq 1d_i$. This agrees with the PDF seen in Fig. 6. The scale-dependent kurtosis for the magnetic field pressure peaks at $\approx 0.1d_i$, that for thermal pressure peaks at $\approx 0.3d_i$, while $\kappa(r)$ of total pressure peaks at $\approx 0.5d_i$, approaching a value closer to 3 for larger lags. This implies that the fluctuations at smaller lags are intermittent, and therefore the original Kolmogorov (1991) similarity hypothesis is not valid and needs some discussion or clarification.

3.2.2 Structure functions

In this subsection, we discuss the higher order structure functions for pressure fluctuations as measured by the increments δP , and compare

them with the higher order velocity and magnetic structure functions. The structure function of order n is defined as:

$$D_P^n(r) = \langle |\delta P(r)|^n \rangle. \quad (14)$$

For Kolmogorov 1991 scaling (K41 from here on), which ignores intermittency, (see Section 2.3) the pressure fluctuation is expected to scale as $\delta P \sim (\delta v)^2$, and therefore the n^{th} order pressure structure function $D_P^n(r) \sim (\delta v)^{2n} \sim r^{2n/3}$. However, this idealization is not expected to be valid for higher-order structure functions because of the non-Gaussian behaviour as seen in Fig. 6. This section explores the lag dependence of the higher-order pressure structure functions in the kinetic plasmas of interest.

The multi-fractal scaling of pressure fluctuations has not been explored as much as the velocity and magnetic field. Some attempts have been made to include intermittency corrections in the pressure scaling (Donzis, Sreenivasan & Yeung 2012), but not for kinetic plasma turbulence as far as we are aware.

For further analysis, first we assume the pressure structure function to take the form

$$D_P^n(r) \sim r^{\zeta_n}, \quad (15)$$

where ζ_n includes the intermittency correction to the K41 scaling (Kolmogorov 1962; Obukhov 1962). We then compute the scaling exponents for our system and compare that with a few intermittency models that are formulated to describe the scaling of velocity structure functions.

One of the first descriptions of intermittency comes from Oboukhov's suggestion that motivated the Kolmogorov refined similarity hypothesis (Kolmogorov 1962; Oboukhov 1962). Specifically Oboukhov reasoned that patchy dissipation might be accounted for if the velocity fluctuation (i.e. increment) depends on the local value of dissipation and exhibits a log-normal distribution. According to this model (K62 from here on), the scaling exponent takes the form

$$\zeta_n^{K62} = \frac{n}{3} + \frac{\mu}{18}(3n - n^2), \quad (16)$$

where μ is the intermittency exponent, whose values typically range between 0.2 and 0.3 (Van Atta & Antonia 1980; Sreenivasan & Kailasath 1993; Davidson 2015).

Another successful model used to describe intermittency is the She and Leveque model (She & Leveque 1994) which assumes a log-Poisson model distribution. In this model, the exponent has the generalized form

$$\zeta_n = \frac{n}{3}(1 - \alpha) + C_0(1 - \beta^{n/3}), \quad (17)$$

where $C_0 = \frac{\alpha}{1-\beta}$ is related to the dimension D of the dissipative eddies through the relation $C_0 = 3 - D$ (Biskamp 2003) and therefore called the co-dimension. The parameter α is the scaling exponent, while β is a characteristic of the intermittency. For hydrodynamic turbulence, because of the quasi-1D structure of thin vortex filaments, the co-dimension $C_0 = 2$. She and Leveque (She & Leveque 1994) further assumed that with Kolmogorov scaling, $\alpha = 2/3$ and $\beta = 2/3$, which yields

$$\zeta_n^{\text{SL}} = \frac{n}{9} + 2 \left[1 - \left(\frac{2}{3} \right)^{n/3} \right]. \quad (18)$$

However, for magnetohydrodynamic turbulence the smallest dissipative structures may be taken to be 2D as we observe from small-scale current sheets. For that case, $C_0 = 1$. With the same $\alpha = 2/3$, we now have $\beta = 1/3$ that yields the scaling exponents (Politano & Pouquet

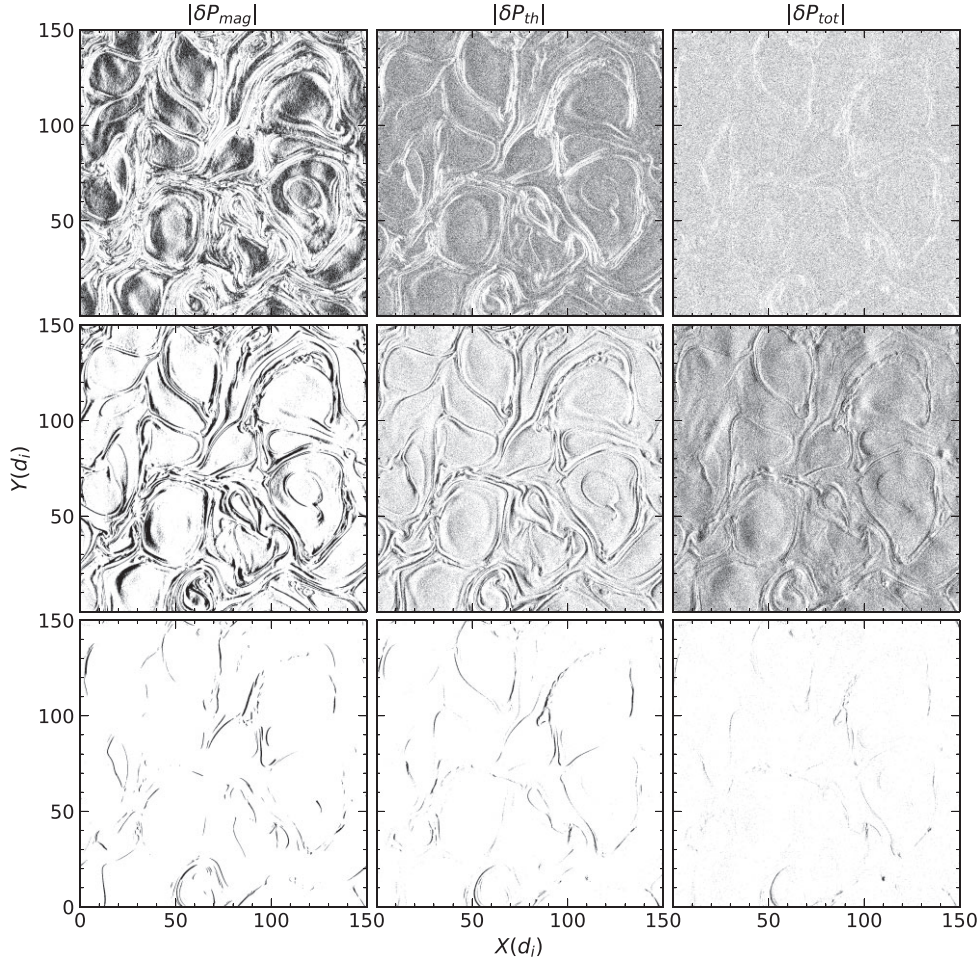


Figure 7. Structures (in black) contributing to regions I, II, and III of the probability density function (PDF) of the magnetic (left column), thermal (middle column), and total pressure (right column) increments shown in Fig. 6 for a lag of $r \approx d_e$, averaged over x and y directions. Each row corresponds to the region shown on the right side of the figure.

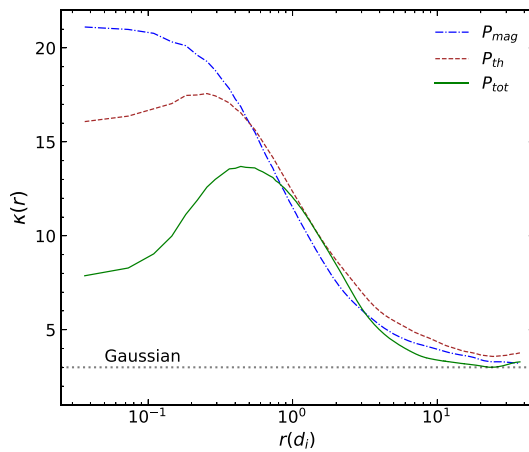


Figure 8. Scale-dependent kurtosis $\kappa(r)$ for magnetic (dash-dot), thermal (dashed), and total pressure (solid) as a function of lag. The dotted line is a reference for the kurtosis of a Gaussian distribution.

1995; Müller & Biskamp 2000) of the form

$$\zeta_n^{\text{MHD}} = \frac{n}{9} + 1 - \left(\frac{1}{3}\right)^{n/3}. \quad (19)$$

Next, in Fig. 9 we show the higher-order structure functions D_p^n versus lag r up to the eighth order. Two vertical lines on the left denote the kinetic range (between $d_e = 0.2d_i$ and $1d_i$), while two vertical lines on the right denote the inertial range (between $4d_i$ and $15d_i$) (Adhikari et al. 2021). The magnitude of the higher-order structure functions is smaller than the lower-order structure functions. The structure functions are observed to be steeper in the kinetic range compared to the inertial range. The steepness of the kinetic range increases sharply with higher-order structure function compared to the inertial range because the fluctuations at those lag scales are much smaller than those in the inertial range. Beyond the inertial range, the structure functions display a similar slope. Next, we calculate the power exponent of these structure functions. In Fig. 10, we plot the scaling exponent of these structure functions as a function of the order n , across the inertial (top) and kinetic (bottom) range and compare it with those from the magnetic and velocity structure functions. The exponents are obtained using power-law fits to the structure function curve at both the inertial and kinetic ranges. It is instructive to compare the present results with similar findings presented for

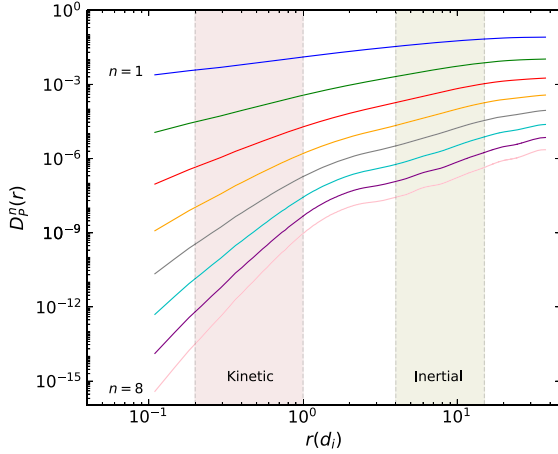


Figure 9. Sequence of higher order structure functions for pressure. For uniformity, we assume that the region between the dashed lines at $d_c = 0.2d_i$ and d_i denotes the kinetic range (brown rectangle), and the region between 4 and $15d_i$ represents the inertial range (olive rectangle) (see Adhikari et al. 2021).

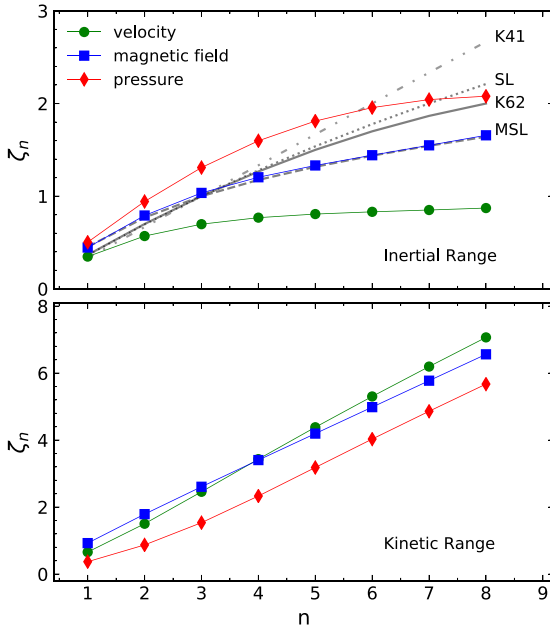


Figure 10. Power index for different orders n of the magnetic (blue squares), velocity (green circles), and pressure (red diamond) structure functions in the inertial (top), and kinetic (bottom) range as defined by the shaded rectangles in Fig. 9. The scaling exponents predicted by different models in the inertial range are drawn for reference (see text for details). In the kinetic range, the scaling exponents follow a linear trend with a slope of 0.927 (velocity), 0.801 (magnetic field), and 0.779 (pressure).

kinetic plasma turbulence by (Wan et al. 2016) and for the density in compressible MHD turbulence by (Yang et al. 2017b).

The scaling exponents for the structure function follow the order velocity < magnetic field < pressure, with the ratio between pressure and velocity structure function ~ 2 . The value of ζ_n for the velocity/magnetic and pressure structure functions decrease more and more from the conventional (K41) value of $n/3$ and $2n/3$, respectively as n increases. Interestingly, the exponent saturates to a value close to 1 for the velocity structure function.

We also plot the K41, SL, and K62 prediction for comparison. Clearly, none of these models fully describe the exponents obtained from our simulations. However, interestingly, the exponent for the magnetic structure functions is in good agreement with the generalized She Leveque exponent (equation 17) with scaling exponent $x = 3/4$, and $\beta = 1/4$, such that the co-dimension $C_0 = 1$. This curve is denoted by modified SL in Fig. 10.

In the kinetic range (bottom panel Fig. 10), the exponents for all the structure functions exhibit a linear relation with the order of the structure function, contrary to the inertial range behaviour. The values of the exponents for lower-order ($n \lesssim 6$) magnetic and velocity structure functions are similar. However, for $n > 6$ the difference in ζ_n starts to increase and diverges with increasing n (not shown). On the contrary, the power exponent for the pressure structure functions is smaller in the kinetic range suggesting that the previous description in the inertial range is not valid in the kinetic range. More studies emphasizing the kinetic regime of the structure functions will certainly shed some light on our understanding of the structure functions.

Recent works on intermittency in the magnetic field provide guidance in this issue, while it remains clear that some subtle distinctions may be needed. For example, Leonardis et al. (2013) found multifractal scaling of the magnetic field at subproton scales in simulations of kinetic reconnection, but also found monofractal Gaussian scaling at scales less than d_i (Leonardis et al. 2016). Other kinetic simulations of collisionless plasma turbulence supported the finding that turbulence at proton scales and smaller is self-similar, i.e. monofractal (Wan et al. 2016). Laboratory findings (e.g. Schaffner & Brown 2015) and Parker Solar Probe data (Chhiber et al. 2021) also find monofractal behaviour at sub-proton scales. Here, we have found very similar results for intermittency in the total pressure. First, we have found that the pressure fluctuations are indeed intermittent. Second, the finding of multifractal scaling at scales larger than d_i , and monofractal scaling at scales less than d_i is in accordance with characterization of magnetic field intermittency in a number of prior studies.

4 CONCLUSIONS

Pressure balance has long been an important element in space plasma physics (Burlaga et al. 1990). The traditional viewpoint adopts explicitly an assumption that fluctuations are small, leading to a menu of linear wave solutions and small amplitude pressure fluctuations that emerge as special static solutions of the MHD equations (Cowling 1976). Here, we have employed particle-in-cell simulations of kinetic turbulence starting from conditions that give rise to strong MHD scale fluctuations and subsequently the formation of strong spatial intermittency, coherent structures, and nonuniform dissipation.

In this paper, we emphasize the properties of pressure fluctuations that are of inherently non-linear and stochastic nature, and therefore the characteristics we describe are attributable to turbulence and not a collection of static or wavelike structures.

The key conclusions of this paper are listed below:

(i) Poisson's equation for pressure (equation 7) in terms of Elsässer's variable was presented. The asymptotic solutions to this equation explains the quasi-pressure balance (Montgomery et al. 1987) obtained in turbulent MHD systems. Similarly, Poisson's equation for the pressure fluctuation is formulated in terms of Elsässer shear (equation 9). The form of the equation is the same as it would be for velocity replaced by Elsässer variables.

(ii) In a PIC simulation of decaying turbulence, as turbulence is fully developed, the volume averaged change in the thermal pressure behaves opposite to that of the magnetic pressure keeping the total pressure nearly constant as seen in Fig. 1. A 2D view of the thermal (ion plus electron) and magnetic pressure indicates the suggested signatures of anti-correlation between the magnetic and the thermal pressure locally, and results in the global anti-correlation (Figs 2 and 3).

(iii) The scales at which the magnetic-thermal pressure anticorrelation dominates are clarified by a direct scale-dependent correlation analysis facilitated by band pass filtering, shown in Fig. 4. The anticorrelation mainly inhabits intermediate scales, and disappears both at the large energy-containing scales and at the small kinetic dissipation scales. The present simulation is not large enough to display an idealized inertial range but this intermediate range does exhibit power-law spectra in the expected range of values. Apparently the result found here, that anticorrelation is dominant at the intermediate ‘inertial range’ scales provides a concrete manifestation of the asymptotic results derived by Montgomery et al. (1987).

(iv) Associated with this anti-correlation, the omnidirectional pressure spectrum has a characteristic slope of $-7/3$ (Fig. 5) in the inertial range while the magnetic and thermal pressure each have a slope of $-5/3$, a less steep power spectrum than the total pressure spectrum. The significant cross contribution between the two pressure terms (magnetic and thermal) is a result of the anti-correlation between the two. This result is also anticipated in the asymptotic calculation of Montgomery et al. (1987).

(v) The intermittent behaviour of pressure fluctuations is discussed and contrasted to the intermittency observed in the velocity and magnetic fields. The ratio of the scaling exponents for the higher-order pressure structure function to that of velocity structure function in the inertial range is ~ 2 . None of the previously described intermittency models fit the scaling exponent obtained from our simulations; resolution of this issue requires detailed study that is outside the scope of this paper. The exponents for velocity structure functions are much lower than the predicted value for higher orders n and saturate close to 1. The scaling exponent for magnetic structure functions does agree with the MHD description of the SL model but with a different scaling exponent. Further, both monofractal and multifractal scaling exponents are observed in the pressure, suggesting that traces of the intermittent behaviour are also observed in pressure fluctuations.

This study sheds light on the contribution of thermal and magnetic pressure to the total pressure using pressure spectra and higher-order statistics. One can use these results to characterize the fluctuations of mass density in many astrophysical systems, exploring the contributions coming from the thermal and magnetic pressure in the system (Lau et al. 2013). Therefore, studies of pressure fluctuations in astrophysical systems can only lead to a better understanding of the system.

Finally it is not yet clear if the findings presented here will extrapolate to more complete or widely applicable models. One issue is that of dimensionality, and the extension of the present results to three dimensions. In that case the expected anisotropy of magnetic fields (Oughton, Priest & Matthaeus 1994) should play a major role. A framework for examining three dimensional effects in weakly compressible MHD was presented in Matthaeus et al. (1991). Even greater is the scope of possible extensions to more complete three-dimensional plasma models, such as weakly collisional Vlasov models (Pezzi et al. 2019) and kinetic-modified MHD models (Kunz et al. 2018; Squire et al. 2023). Such models

have the capacity to take into account the important topic of pressure anisotropy. Indeed pressure anisotropy can drive instabilities that are well understood to be significant in both astrophysics (Squire et al. 2017) and heliospheric physics (Matteini et al. 2007). Given the great variation in physical processes that occur in widely different models of three-dimensional plasma turbulence, it is also not clear if the conclusions present here will prove to be universal across all attainable parameters. Future studies on these extensions are therefore warranted.

ACKNOWLEDGEMENTS

SA acknowledges helpful discussions with Francesco Pecora. All the authors would like to acknowledge the high-performance computing support from Cheyenne (Computational and Information Systems Laboratory 2017) provided by NCAR’s Computational and Information Systems Laboratory, sponsored by the NSF. We also thank NERSC resources, a U.S. DOE Office of Science User Facility operated under Contract No. DE-AC02-05CH11231. SA and MAS acknowledge support from NASA LWS 80NSSC20K0198. PAC gratefully acknowledges the hospitality from the University of Delaware and the Bartol Research Institute during his sabbatical visit, and acknowledges support from NASA Grant No. 80NSSC19M0146, and the Bartol Research Institute. SA and PAC are also supported by DOE grant DE-SC0020294. WHM is supported by NSFDOE grant AGS 2108834 at the University of Delaware, the IMAP project (Princeton subcontract SUB0000317) and the NASA LWS programme FST grant to New Mexico Consortium (subcontract 655–001 to Delaware).

DATA AVAILABILITY

The data that support the findings of this study are openly available in Zenodo (Adhikari et al. 2023).

REFERENCES

- Adhikari S., Parashar T., Shay M., Matthaeus W., Pyakurel P., Fordin S., Stawarz J., Eastwood J., 2021, *Phys. Rev. E*, 104, 065206
- Adhikari S., Matthaeus W. H., Parashar T. N., Shay M. A., Cassak P. A., 2023, *Simulation dataset for "Statistics of Pressure Fluctuations in Turbulent Kinetic Plasmas" [Data set]*. Zenodo. Available at: <https://doi.org/10.5281/zenodo.7776539>
- Angelini M., Vazza F., Giocoli C., Etori S., Jones T., Brunetti G., Brüggemann M., Eckert D., 2020, *MNRAS*, 495, 864
- Armstrong J., Cordes J., Rickett B., 1981, *Nature*, 291, 561
- Arzamasskiy L., Kunz M. W., Squire J., Quataert E., Schekochihin A. A., 2023, *Phys. Rev. X*, 13, 021014
- Balbus S. A., Hawley J. F., 1998, *Rev. Mod. Phys.*, 70, 1
- Bale S., Kasper J., Howes G., Quataert E., Salem C., Sundkvist D., 2009, *Phys. Rev. Lett.*, 103, 211101
- Batchelor G., 1951, *Math. Proc. Camb. Phil. Soc.*, 47, 359
- Bayly B. J., Levermore C. D., Passot T., 1992, *Phys. Fluids A*, 4, 945
- Biskamp D., 2003, *Magnetohydrodynamic Turbulence*. Cambridge Univ. Press, Cambridge
- Bott A., Arzamasskiy L., Kunz M., Quataert E., Squire J., 2021, *ApJ*, 922, L35
- Bruno R., Carbone V., 2013, *Living Rev. Sol. Phys.*, 10, 1
- Burlaga L., Scudder J., Klein L., Isenberg P., 1990, *J. Geophys. Res.: Space Phys.*, 95, 2229
- Carlberg R. et al., 1997, *ApJ*, 485, L13
- Chhiber R., Matthaeus W. H., Bowen T. A., Bale S. D., 2021, *ApJ*, 911, L7
- Churazov E. et al., 2012, *MNRAS*, 421, 1123

- Cohen I., Huang Y., Chen J., Benesty J., 2009, *Noise Reduction in Speech Processing*. Springer Berlin Heidelberg, New York, p. 1
- Coleman P. J., Jr, 1968, *ApJ*, 153, 371
- Computational and Information Systems Laboratory, 2017, Cheyenne: HPE/SGI ICE XA System (University Community Computing)
- Cowling T. G., 1976, *Monographs on Astronomical Subjects*. Adam Hilger Ltd., Bristol
- Davidson P. A., 2015, *Turbulence: An Introduction for Scientists and Engineers*. Oxford University Press, Oxford
- Donzis D., Sreenivasan K., Yeung P., 2012, *Physica D*, 241, 164
- Gary S. P., 1993, *Theory of Space Plasma Microinstabilities*. Cambridge Univ. Press, Cambridge
- George W. K., Beuther P. D., Arndt R. E., 1984, *J. Fluid Mech.*, 148, 155
- Germano M., 1992, *J. Fluid Mech.*, 238, 325
- Goldstein M. L., Roberts D. A., Matthaeus W., 1995, *ARA&A*, 33, 283
- Greco A., Matthaeus W. H., Servidio S., Chuychai P., Dmitruk P., 2009, *ApJ*, 691, L111
- Hellinger P., Trávníček P. M., Štverák Š., Matteini L., Velli M., 2013, *J. Geophys. Res.: Space Phys.*, 118, 1351
- Higdon J. C., 1984, *ApJ*, 285, 109
- Hill R. J., Boratav O. N., 1997, *Phys. Rev. E*, 56, R2363
- Hill R. J., Boratav O. N., 2001, *Phys. Fluids*, 13, 276
- Hill R. J., Wilczak J. M., 1995, *J. Fluid Mech.*, 296, 247
- Khatri R., Gaspari M., 2016, *MNRAS*, 463, 655
- Kim J., Antonia R., 1993, *J. Fluid Mech.*, 251, 219
- Klainerman S., Majda A., 1981, *Commun. Pure Appl. Math.*, 34, 481
- Kolmogorov A. N., 1962, *J. Fluid Mech.*, 13, 82
- Kolmogorov A. N., 1991, *Proc. R. Soc. A*, 434, 9
- Kravtsov A. V., Borgani S., 2012, *ARA&A*, 50, 353
- Kunz M. W., Abel I. G., Klein K. G., Schekochihin A. A., 2018, *J. Plasma Phys.*, 84, 715840201
- Lau E. T., Nagai D., Nelson K., 2013, *ApJ*, 777, 151
- Leamon R. J., Smith C. W., Ness N. F., Matthaeus W. H., Wong H. K., 1998, *J. Geophys. Res.*, 103, 4775
- Leonardis E., Chapman S. C., Daughton W., Roytershteyn V., Karimabadi H., 2013, *Phys. Rev. Lett.*, 110, 205002
- Leonardis E., Sorriso-Valvo L., Valentini F., Servidio S., Carbone F., Veltri P., 2016, *Phys. Plasmas*, 23, 022307
- Ley F., Zweibel E. G., Riquelme M., Sironi L., Miller D., Tran A., 2023, *ApJ*, 947, 89
- Markevitch M., Gonzalez A., Clowe D., Vikhlinin A., Forman W., Jones C., Murray S., Tucker W., 2004, *ApJ*, 606, 819
- Matteini L., Landi S., Hellinger P., Pantellini F., Maksimovic M., Velli M., Goldstein B. E., Marsch E., 2007, *Geophys. Res. Lett.*, 34, L20105
- Matthaeus W. H., Brown M. R., 1988a, *Phys. Fluids*, 31, 3634
- Matthaeus W. H., Brown M. R., 1988b, *Phys. Fluids*, 31, 3634
- Matthaeus W. H., Goldstein M. L., 1982, *J. Geophys. Res.: Space Phys.*, 87, 6011
- Matthaeus W. H., Klein L. W., Ghosh S., Brown M. R., 1991, *J. Geophys. Res.: Space Phys.*, 96, 5421
- Monin A., Yaglom A., 1975, *Statistical Fluid Mechanics: Mechanics of Turbulence*. Vol. 2, MIT Press, Cambridge, MA
- Montgomery D., Brown M. R., Matthaeus W., 1987, *J. Geophys. Res.: Space Phys.*, 92, 282
- Müller W.-C., Biskamp D., 2000, *Phys. Rev. Lett.*, 84, 475
- Nelkin M., Chen S., 1998, *Phys. Fluids*, 10, 2119
- Oboukhov A. M., 1962, *J. Fluid Mech.*, 13, 77
- Obukhoff A., Yaglom A., 1951, *NACA Tech. Mem.*, 1350
- Obukhov A. M., 1962, *J. Geophys. Res.*, 67, 3011
- Oughton S., Priest E. R., Matthaeus W. H., 1994, *J. Fluid Mech.*, 280, 95
- Parashar T. N., Matthaeus W. H., 2016, *ApJ*, 832, 57
- Parashar T. N., Matthaeus W. H., Shay M. A., 2018, *ApJ*, 864, L21
- Pessah M. E., 2010, *ApJ*, 716, 1012
- Pezzi O., Perrone D., Servidio S., Valentini F., Sorriso-Valvo L., Veltri P., 2019, *ApJ*, 887, 208
- Planells S., Schleicher D., Bykov A., 2015, *Space Sci. Rev.*, 188, 93
- Politano H., Pouquet A., 1995, *Phys. Rev. E*, 52, 636
- Pratt G., Arnaud M., Biviano A., Eckert D., Etori S., Nagai D., Okabe N., Reiprich T., 2019, *Space Sci. Rev.*, 215, 1
- Pullin D., Rogallo R., 1994, *Proc. 1994 Summer Program, Studying Turbulence Using Numerical Simulation Databases*. 5. Stanford Univ., Stanford, CA
- Qudsi R. A. et al., 2020, *ApJ*, 895, 83
- Reisenfeld D. B., McComas D., Steinberg J., 1999, *Geophys. Res. Lett.*, 26, 1805
- Ruffolo D., Ngampoopun N., Bhora Y. R., Thepthong P., Pongkitiwanichakul P., Matthaeus W. H., Chhiber R., 2021, *ApJ*, 923, 158
- Sahraoui F., Hadid L., Huang S., 2020, *Rev. Mod. Plasma Phys.*, 4, 1
- Schaffner D., Brown M. R., 2015, *ApJ*, 811, 61
- Schuecker P., Finoguenov A., Miniati F., Böhringer H., Briel U., 2004, *A&A*, 426, 387
- Schumann U., Patterson G., 1978, *J. Fluid Mech.*, 88, 685
- Servidio S., Matthaeus W., Dmitruk P., 2008, *Phys. Rev. Lett.*, 100, 095005
- She Z.-S., Leveque E., 1994, *Phys. Rev. Lett.*, 72, 336
- Simionescu A. et al., 2019, *Space Sci. Rev.*, 215, 1
- Smith C. W., Hamilton K., Vasquez B. J., Leamon R. J., 2006, *ApJ*, 645, L85
- Squire J., Quataert E., Kunz M. W., 2017, *J. Plasma Phys.*, 83, 905830613
- Squire J., Kunz M. W., Arzamasskiy L., Johnston Z., Quataert E., Schekochihin A. A., 2023, *J. Plasma Phys.*, 89, 905890417
- Sreenivasan K., Kailasnath P., 1993, *Phys. Fluids A*, 5, 512
- Swisdak M., 2016, *Geophys. Res. Lett.*, 43, 43
- Tran A., Sironi L., Ley F., Zweibel E. G., Riquelme M. A., 2023, *ApJ*, 948, 130
- Tsuji Y., Ishihara T., 2003, *Phys. Rev. E*, 68, 026309
- Uberoi M. S., 1953, *J. Aeronaut. Sci.*, 20, 197
- Van Atta C., Antonia R., 1980, *Phys. Fluids*, 23, 252
- Vellante M., Lazarus A., 1987, *J. Geophys. Res.: Space Phys.*, 92, 9893
- Verscharen D., Klein K. G., Maruca B. A., 2019, *Living Rev. Sol. Phys.*, 16, 5
- Voigt L., Fabian A., 2006, *MNRAS*, 368, 518
- Wan M., Matthaeus W. H., Roytershteyn V., Parashar T. N., Wu P., Karimabadi H., 2016, *Phys. Plasmas*, 23, 042307
- Wang C., Richardson J., 2001, *J. Geophys. Res.: Space Phys.*, 106, 29401
- Wang Y. et al., 2022, *ApJ*, 937, 76
- Yang Y. et al., 2017a, *Phys. Plasmas*, 24, 072306
- Yang Y., Matthaeus W. H., Shi Y., Wan M., Chen S., 2017b, *Phys. Fluids*, 29, 035105
- Yang Y., Matthaeus W. H., Roy S., Roytershteyn V., Parashar T. N., Bandyopadhyay R., Wan M., 2022, *ApJ*, 929, 142
- Yang Y. et al., 2023, *ApJ*, 944, 148
- Zank G. P., Matthaeus W. H., 1990, *Phys. Rev. Lett.*, 64, 1243
- Zank G. P., Matthaeus W. H., 1992, *J. Geophys. Res.*, 97, 17
- Zank G. P., Matthaeus W. H., 1993, *Phys. Fluids A*, 5, 257
- Zeiler A., Biskamp D., Drake J., Rogers B., Shay M., Scholer M., 2002, *J. Geophys. Res.: Space Phys.*, 107, SMP-6
- Zhao S., Cheng E., Qiu X., Burnett I., Liu J. C.-c., 2016, *J. Acoust. Soc. Am.*, 140, 4178
- Zhuravleva I. et al., 2014, *Nature*, 515, 85
- Zhuravleva I., Churazov E., Schekochihin A., Allen S., Vikhlinin A., Werner N., 2019, *Nat. Astron.*, 3, 832

APPENDIX A: SYSTEM OVERVIEW

Fig. A1 provides an overview of the simulation at the time of analysis ($t = 116.5\omega_{ci}^{-1}$). The magnitude of the out-of-plane current $|j_z|$ distinguishes the current sheets from the magnetic islands.

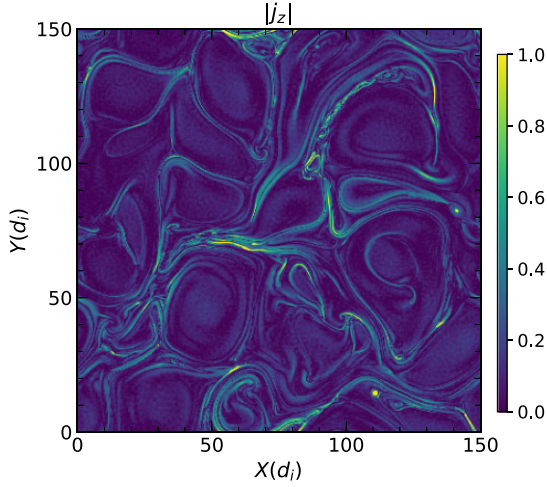


Figure A1. Magnitude of the out-of-plane current density j_z at the time of analysis ($t\omega_{ci} = 116.5$). The current sheets are the regions with larger magnitudes of j_z .

APPENDIX B: PRESSURE ANISOTROPY

In this subsection, we explore the thermal pressure anisotropy and examine its role in the overall pressure balance. Fig. B1 shows the ratio of the perpendicular to the parallel thermal pressure for each species of electrons and ions and compares it with the total thermal pressure anisotropy. The parallel pressure is defined relative to the local magnetic field and calculated from the pressure tensor \mathbf{P} using $P_{||} = \hat{\mathbf{b}} \cdot \mathbf{P} \cdot \hat{\mathbf{b}}$, where $\hat{\mathbf{b}} = \mathbf{B}/|\mathbf{B}|$ is a unit vector in the direction of the magnetic field (Swisdak 2016). It is immediately evident that the pressure anisotropies are intermittent. The most anisotropic regions are near intense current sheets, and the edges of magnetic islands (Parashar & Matthaeus 2016). The pressure anisotropies of ions and electrons are opposite in the most intense locations, leading to a partial cancellation of overall anisotropy for the total pressure in these locations. This is also an example of the partial cancellation of

forces, an effect that leads to suppression of non-linearity (Servidio et al. 2008). The intermediate anisotropy locations, away from the most intense current sheets, are similar for both species. The global anisotropy (system averaged) for electrons, ions, and the total thermal pressure shown in Fig. B1 support the opposite trend in ion-electron heating.

Fig. B2 shows an enlarged image of the part of the domain where the anti-correlation between the ion and electron pressure anisotropy is clearly observed. However, since the anti-correlation is not exactly pointwise, there exists anisotropy in the total thermal pressure as seen in the right panel of Fig. B2.

Next, we look into joint pdf between the magnetic pressure fluctuations and the perpendicular P_{th}^{\perp} and parallel $P_{th}^{||}$ thermal pressure fluctuations separately in Fig. B3. The perpendicular and parallel thermal pressure display a trend of negative correlation with the magnetic pressure as the joint distribution aligns with the dashed line of slope -1 . However, in terms of Pearson's correlation measure, the correlation coefficient scales as $r_P(P_{mag}, P_{th}^{||}) < r_P(P_{mag}, P_{th}^{\perp}) < r_P(P_{mag}, P_{th})$. The stronger global anti-correlation between magnetic and parallel components of the thermal pressure is primarily due to the parallel heating of the magnetized electrons in the intermittent locations. Next, we look into the scale dependence of the correlation coefficients between (P_{\perp}, P_{mag}) , and $(P_{||}, P_{mag})$ in Fig. B4. Clearly, at scales $\sim d_i$, both P_{\perp} and $P_{||}$ have significant anti-correlation with the magnetic pressure suggesting that the pressure balance observed is aided by both perpendicular and parallel thermal pressure. However, exploring the effect of change in pressure anisotropy to the pressure balance is left for a future study.

Finally, in Fig. B5 we plot the power spectra for the parallel $E_{P_{th}^{\perp}}$ and perpendicular thermal pressure $E_{P_{th}^{||}}$ and compare it with the total thermal pressure spectrum $E_{P_{th}}$. We find that $E_{P_{th}^{\perp}}$ mostly follows $E_{P_{th}}$, while a slight deviation is observed with $E_{P_{th}^{||}}$. Nevertheless, both the perpendicular and parallel components have a slope comparable to $-5/3$ in the inertial range. This suggests that even though some amount of pressure anisotropy exists in the system, this does not change our conclusion about the thermal pressure and the overall pressure balance.

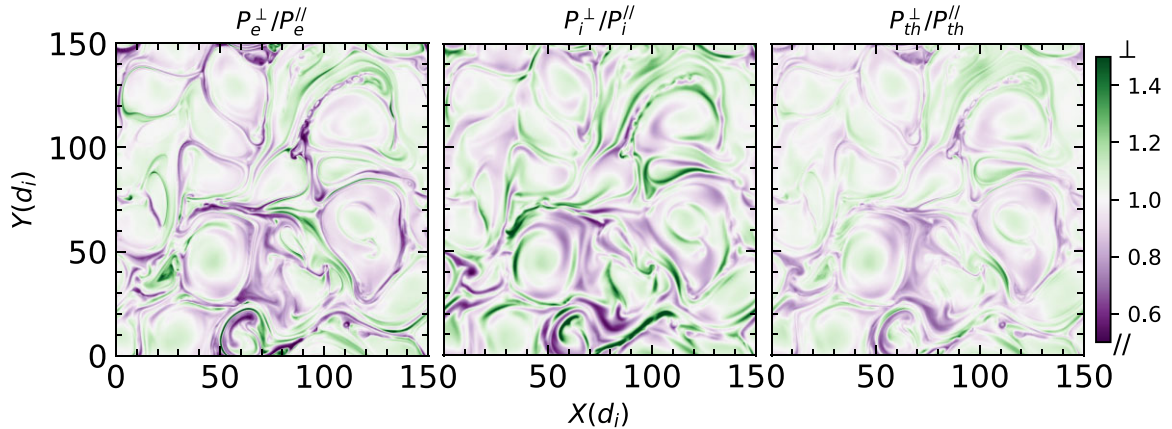


Figure B1. Thermal pressure anisotropy ($P^{\perp}/P^{||}$) observed in individual species of electrons (left) and ions (middle), compared to the total thermal (ions plus electrons) anisotropy (right). The \perp and $||$ in the colour bar are drawn for convenience. The average value of pressure anisotropy for electrons, ions, and the total thermal pressure are 0.989, 1.012, and 0.994, respectively.

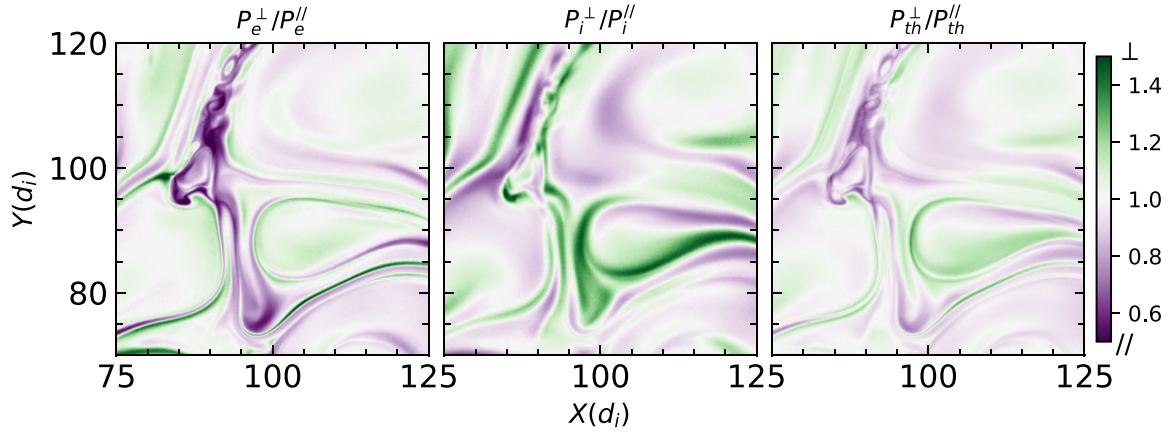


Figure B2. A zoomed in version of Fig. B1 showing the opposite trends in ions and electrons anisotropies. As a result, the anisotropy in the total thermal pressure is smaller and relatively less significant.

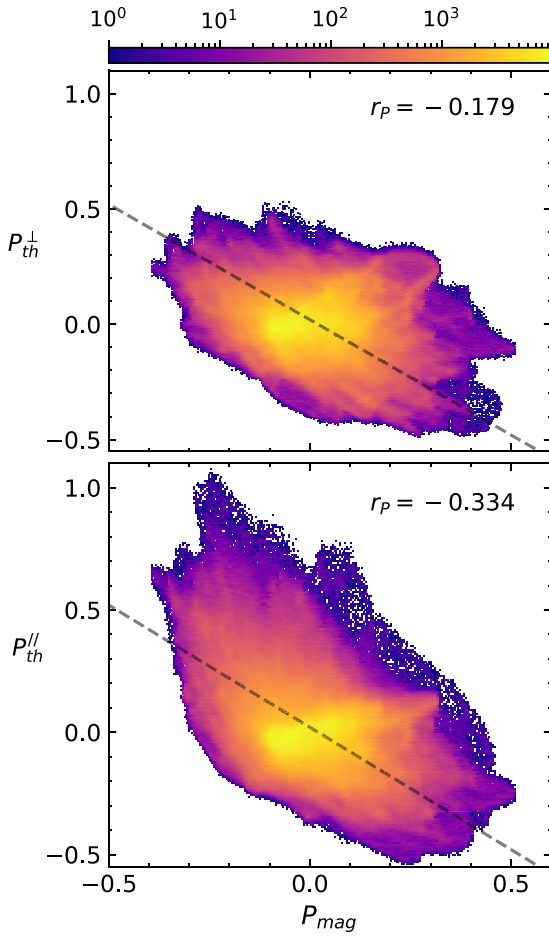


Figure B3. Joint PDFs of the perpendicular, parallel, and total thermal pressure with the magnetic pressure. The Pearson's correlation coefficient calculated for these joint PDFs are -0.179 (top), and -0.334 (bottom).

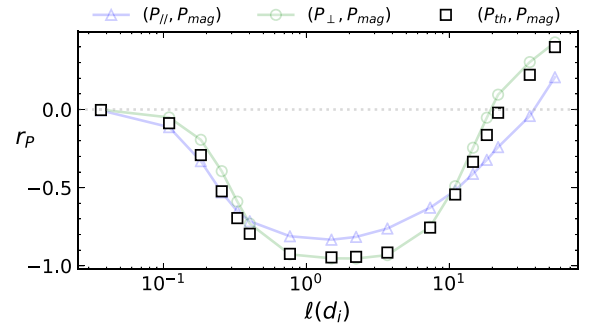


Figure B4. Pearson correlation coefficient r_P between the magnetic pressure and the parallel, and perpendicular thermal pressure as a function of scales.

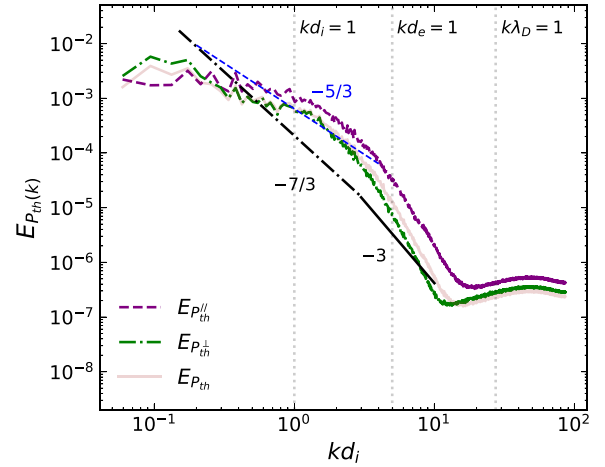


Figure B5. Power spectra for the perpendicular P_{th}^\perp , parallel P_{th}^\parallel and the total thermal pressure P_{th} with lines of slope $-7/3$, $-5/3$, and -3 drawn for reference.

This paper has been typeset from a \LaTeX file prepared by the author.